

Large eddy simulation of flow around semi-conical piers vertically mounted on the bed

Yasin Aghaee-Shalmani (✉ y.ghaee@iaukhsh.ac.ir)

Islamic Azad University of Khomeinishahr

Habib Hakimzadeh

Sahand University of Technology

Research Article

Keywords: Semi-conical piers, Horseshoe vortex, Flow, Numerical model, LES

Posted Date: July 9th, 2021

DOI: <https://doi.org/10.21203/rs.3.rs-698389/v1>

License:   This work is licensed under a Creative Commons Attribution 4.0 International License.

[Read Full License](#)

Large eddy simulation of flow around semi-conical piers vertically mounted on the bed

Yasin Aghaee-Shalmani · Habib Hakimzadeh

Received: date / Accepted: date

Abstract In this paper, details, and results of three-dimensional numerical modeling of flow around the semi-conical piers vertically mounted on the bed in a channel, are presented. For flow simulation, 3-D Navier-Stokes equations are solved numerically using the finite volume method and large eddy simulation (LES). In this study, the semi-conical piers with different side slope angles are tested, and the flow around them is compared with the cylindrical reference pier. Flow structures, vortex shedding behind piers, horseshoe vortices, instantaneous and time-averaged flow structures are presented and discussed. Numerical model results show that the semi-conical piers are eventuated remarkable reduction (up to 25%) in downward flow velocity in the upstream side of the piers, and much more reduction (up to 46%) in bed shear stresses in comparison with the cylindrical pier. Moreover, the model results showed some decrease in vortex shedding frequency for the semi-conical piers compared to the cylindrical pier.

Keywords Semi-conical piers · Horseshoe vortex · Flow · Numerical model · LES

1 Article Highlights

We report on numerical results of large eddy simulation of the flow around semi-conical piers with different side slopes. This research is significant because of the effect of these piers on the:

- reduction of the downward flow and the bed shear stress around the piers.
- reduction of vortex shedding frequency for the semi-conical piers compared to the cylinder.
- different behavior of the horseshoe vortices at the upstream compared to the cylinder.

F. Author
Department of Mechanical and Civil Engineering, Khomeinishahr Branch, Islamic Azad University, Khomeinishahr, Iran
Tel.: +98-33660011
E-mail: y.ghaee@iaukhsh.ac.ir
orcid=0000-0003-4655-6023

S. Author
Department of Civil Engineering, Sahand University of Technology, Tabriz, Iran

2 Introduction

Numerous researchers have already investigated the flow structures and scour process around piers experimentally. Among them, Baker (1980); Dargahi (1990, 1989); Dey and Raikar (2007); Unger and Hager (2007) studied the horseshoe vortices and flow structures around piers. The horseshoe vortex (HV) has a significant effect on the scour process. At the location of the horseshoe vortex, the increase of bed shear stress and turbulence intensity is evident (Dargahi, 1989; Guan et al., 2019). Horseshoe vortices are mainly generated by down-flow and separation of the flow upstream of the pier. The turbulence intensity and the increased bed shear stress within the HV system carry the sediment particles and develop the local scour around the pier (Gazi and Afzal, 2020).

The shape and the size of the pier have substantial impacts on the size and strength of the horseshoe vortices. Regarding the form of the pier, one of the parameters that affect the horseshoe vortices is the lateral slopes of the pier. The effect of this parameter can also be seen in scour depth for such piers. Bozkus and Yildiz (2004); Vaghefi et al. (2016) reported reducing scour depth for inclined pier toward the downstream. Sumer et al. (1995); Fredsøe and Sumer (1997); Pourahmadi and Hakimzadeh (2011); Aghaee-Shalmani and Hakimzadeh (2015) in their experimental studies have shown that the semi-conical piers can reduce the scour depth.

Sumer et al. (1995) indicated that the bed shear stresses around cone-shaped piers are decreased as the side slopes are increased, and robustness of the horseshoe vortices are mainly reduced compared to a circular cylinder (Sumer et al., 1995). To investigate the scour phenomenon, understanding the flow pattern and its effect on the shear stress of the bed is crucial. Ouro et al. (2017), in numerical and experimental research, studied the flow around the conical island with a large side angle in shallow water conditions and the flow structures around the cone, including the recirculation region, vortex shedding, and separated shear layers were discussed. To the best of our knowledge, there are a few studies of flow around semi-conical piers with small side slope angles in currents. Existent experimental studies of flow around semi-conical piers relevant to investigating the flow structures and vortex shedding behind them and are almost restricted to the very tall and slim cylinders without interactions from the walls (Hsiao and Chiang, 1998; Hsiao et al., 1993). These experiments are relevant to aircraft or missile industrial investigations (Hsiao and Chiang, 1998). The vortex shedding with cellular patterns and frequency of wakes have been studied in the mentioned researches.

The experimental investigations of flow around hydraulic structures are almost expensive and sometimes inaccessible. For this reason, the numerical modeling of the flow can reveal more information about turbulent flows around hydraulic structures like piers. Most of the available numerical simulations of the flow and scour around piers have been carried out using Reynolds averaged Navier-Stokes equations models (RANS) (Olsen and Melaaen, 1993; Salaheldin et al., 2004; Nagata et al., 2005; Afzal et al., 2020). RANS methods compared to the large eddy simulation (LES) method are not successful enough to predict some of the flow characteristics around bluff bodies. (Rodi, 1997; Cheng et al., 2003; Aghaee and Hakimzadeh, 2010). Also, direct numerical simulation (DNS) of turbulent flows is too expensive and time-consuming (Rodi, 2006). Therefore, LES is a reliable and efficient method to solve the turbulent flows at moderate or high Reynolds numbers.

Kirkil et al. (2008), in a numerical study, modeled the flow around the cylinder on a scoured bed using LES. Also, Paik et al. (2007); Kirkil et al. (2009) simulated the turbulent flow around a pier at high Reynolds numbers using detached eddy simulation (DES). In low and medium Reynolds numbers, the LES method is possible without wall function and

with the appropriate number of grids (Kirkil et al., 2008, 2009). Kirkil and Constantinescu (2012) used LES to investigate the flow around vertical cylinders and the laminar horseshoe vortices around them. Effects of Various Reynolds number (between high and low) on the flow structure, turbulence, and behavior of horseshoe vortices (HV) has been investigated comprehensively with particle image velocimetry (PIV), and numerical modeling DES by Kirkil and Constantinescu (2015). Zhang et al. (2020) developed a finite volume code for modeling the flow and scour around the cylinder using LES, and the form and strength of the HV during the scour process were explained.

To the best of our knowledge, there is not any detailed numerical study about the turbulent flow around semi-conical (tapered) piers mounted on the bed. In this study, the turbulent flow around semi-conical piers vertically mounted on the bed has been studied numerically using LES. Governing equations were numerically solved using the finite volume and artificial compressibility methods. To solve the equations in time, the dual-time stepping method was used. The flow regime in the channel was subcritical, and the Reynolds number of the flow based on the free stream velocity, pier diameter, and fluid viscosity was turbulent. The bed was assumed fixed and straight with no sediment movements. The rigid-lid assumption was applied for water free-surface.

The focus of this study is on the flow structure around tapered piers with different side slopes. Since the horseshoe vortices and wakes behind piers are important in the scour process, the bed shear stresses and frequency of vortex shedding, and the properties of the horseshoe vortex are discussed. The importance of the present study is because of the shortage of data about flow structure around semi-conical piers mounted on the bed. This study may reveal some auxiliary information on this issue.

3 Numerical Method

In this work, the governing equations of flow are Navier-Stokes equations. The equations were discretized using the finite volume method, and LES was adopted to simulate turbulent flow using the Smagorinsky model. The artificial compressibility method (AC) with dual-time stepping was used to solve the discretized unsteady flow equations (Breuer and Hänel, 1993; Kim and Menon, 1999; Fu et al., 2009). The form of the filtered Navier-Stokes equations based on the LES and dual-time stepping AC is as follows:

$$\frac{1}{\rho\beta^2} \frac{\partial \bar{p}}{\partial \tau} + \frac{\partial \bar{u}_i}{\partial x_i} = 0, \quad (1)$$

$$\frac{\partial \bar{u}_i}{\partial \tau} + \frac{\partial \bar{u}_i}{\partial t} + \frac{\partial \bar{u}_i \bar{u}_j}{\partial x_i x_j} = -\frac{1}{\rho} \frac{\partial \bar{p}}{\partial x_i} + \nu \frac{\partial^2 \bar{u}_i}{\partial x_j \partial x_j} - \frac{\partial \tau_{ij}}{\partial x_j}, \quad (2)$$

Where x_i are the Cartesian coordinates, ρ is the fluid density, p is the pressure, and ν is the kinematic viscosity of the fluid. τ_{ij} is the sub-grid turbulence stress, and the overbar shows the spatial filtering; t is the real-time, and τ is the artificial (pseudo)-time. In the dual-time stepping method, instead of solving each time step in real-time, the problem is transformed into a sequence of steady-state computations in artificial times. β is the artificial compressibility parameter, and its value was adopted equal to inlet flow velocity in the computational domain (Aghaee and Hakimzadeh, 2010; Aghaee-Shalmani and Hakimzadeh, 2016).

Filtering operation separates the solution to resolved large scales and sub-grid scale, which is unresolved and must be modeled. The simplest model for modeling the sub-grid scales of turbulence (Smagorinsky) was used in this study. τ_{ij} , represents the contribution

from the sub-grid scales and must be modeled to close the system of equations. The eddy viscosity concept for the sub-grid stress is:

$$\tau_{ij} - \frac{1}{3}\tau_{kk}\delta_{ij} = -2\nu_t\bar{S}_{ij}, \quad \nu_t = l_s^2|\bar{S}_{ij}|, \quad (3)$$

where ν_t is the sub-grid eddy-viscosity coefficient, and δ_{ij} is the Kronecker delta. \bar{S}_{ij} is the strain rate tensor for the resolved scale and l_s is the sub-grid length scale. l_s depends on the grid size and Smagorinsky constant parameter (C_s),

$$l_s = \min(\kappa y, C_s \Delta^{\frac{1}{3}}), \quad (4)$$

Δ is the volume of the computational cell, κ is the Vonkarmann constant, and y is the distance to the nearest wall. C_s is the sub-grid scale parameter. The value of C_s depends on the problem. However, the large values of C_s cause excessive damping of the large-scale fluctuations, and very small values ($C_s < 0.1$) may cause convergence problems (Lam and Lin, 2008). The optimum values of the C_s can be found in the literature as $0.1 < C_s < 0.14$. In this research, the parameter C_s was adopted as 0.11.

The momentum interpolation method (MIM) used by Cubero and Fueyo (2007) was applied to overcome the pressure oscillation due to the collocated grid. Time discretizations of the equations were carried out using the implicit first-order forward Euler method for virtual time and backward second order for real-time. Convective terms were discretized using the QUICK scheme. The differenced correction method of Khosla and Rubin (1974) was used to deal with convective terms in implicit discretization. The implicit part of the convective terms was linearized by the Newton method (Sheu and Lin, 2004). Viscous terms were discretized using the second-order central scheme, and the pressure gradient was approximated by the central scheme. The implicit point Gauss-Seidel method with under relaxation was then applied to solve the linearized system with a seven-diagonal matrix. The values of the physical time step (Δt) and artificial time step ($\Delta \tau$) depend on the discretization scheme. This backward differencing scheme is strongly stable and dissipative, and thus it is nearly insensitive to the stiffness of the problem (Kim and Menon, 1999). The decomposition of the computational domain to equally spaced partitions was carried out to equally divide the computational cost between processors using the message passing interface method (MPI) to transfer data between the processors. For every run, 16 to 20 processors were used in the simulations. Because of using the QUICK method for convective terms and the momentum interpolation method, it was needed to pass the data of two layers of the decomposed domains between two adjacent domains (processors). The messages were sent using non-blocking send and receive MPI functions. The solver code has been applied to internal and external flows like cavity flow and flow around a vertical cylinder. For more details of the numerical method and verification of the numerical model, refer to Aghaee and Hakimzadeh (2010); Aghaee-Shalmani and Hakimzadeh (2016).

3.1 Computational domain and boundary conditions

The flow past semi-conical piers vertically mounted on the bed was simulated based on the configurations in the experimental study of flow and scour around semi-conical piers by Aghaee-Shalmani and Hakimzadeh (2015). Semi-conical piers with various side slopes $\alpha = 0^\circ, 5^\circ, 10^\circ$ and 15° were tested in the numerical model. A schematic view of the numerical domain and a semi-conical pier are depicted in Fig. 1. The length of the computational domain was $20D$, where D is the mean pier diameter of the piers.

The computational domain was discretized by an O-type mesh, created by an elliptic Poisson differential equation to adjust the grid size contraction around the piers. The O-type mesh is a usual type of mesh for modeling flow around cylinders or bluff bodies (Gushchin et al., 2002; Kitagawa and Ohta, 2008; Labbé and Wilson, 2007).

Also, the clustering of the grids was carried out near the bed with a hyperbolic mesh generator. The computational domain length in the present study was long enough at the upstream of the pier to allow the current to become fully developed. The logarithmic velocity distribution of the flow at the inlet ensures that the flow is fully developed over a short length at the upstream of the piers. Different grids were tested for simulation, and 160×160 for the horizontal plane, and 64 grids were chosen for flow depth. A logarithmic flow distribution was applied at the inlet, and the convective boundary condition at the outlet was used to ensure no reflection from the outlet.

The inlet boundary was located at the left half of the domain, and the outlet was located at the right half. The mean flow velocity at the inlet was about 0.19 m s^{-1} , and the flow depth was set to be 0.1 m. The boundary condition at the bed and the pier's surface was the no-slip condition, and at the top of the flow, the rigid-lid assumption was applied. The rigid lid assumption for the free surface at low Froude number ($F < 0.2$) is acceptable due to too small bow wave height in front of the pier (Roulund et al., 2005; Kirkil et al., 2009; Kirkil and Constantinescu, 2012). For assessing this claim, the flow with free-surface and rigid-lid assumptions across the semi-conical piers ($\alpha = 0^\circ$ and 10°) were tested. No meaning differences were found in comparisons (the numerical results are not shown here for brevity).

Based on the grids in the present study, the smallest grids size near the bed has a non-dimensional length of about $z/D = 1.06 \times 10^{-3}$, equivalent to $z^+ = \frac{u_* z}{\nu} = 1 \sim 3$. Where u_* is the bed shear velocity, z is the distance of the center of the first off-wall computational cell from the rigid wall, and ν is the kinematic viscosity of the fluid. It seems that this resolution for grids is adequate for LES modeling. The maximum grid size in the flow depth was about 25 wall units close to the free surface.

Table. 1 presents the detail of the used semi-conical piers and flows conditions. In this table, D_1 and D_2 are the upper and lower base diameters of the semi-conical pier at the free-surface and bed levels, respectively. Moreover, D is the mean diameter of the semi-conical pier ($D = (D_1 + D_2)/2$) (see Fig. 1). The flow depth was $h = 2.5D$ for all of the tests. The side slope angle of the conical piers was calculated as $\alpha = \tan^{-1}(D_2 - D_1)/2h$, and equal to $\alpha = 0^\circ, 5^\circ, 10^\circ$, and 15° . The Reynolds number based on the mean diameter of piers (R_D) was about 8,000.

4 Numerical model Results

4.1 Time-Averaged values

Flow around a cylinder is entirely three-dimensional and complex, especially near the up-or downstream side of the cylinder. There are significant temporal variations in vortices and the structure of 3D flow and horseshoe vortex. The time-averaging process is needed to compare the results with each other, along with the most temporal variations in the flow structure. For the present study, time-averaged quantities are obtained for about 20 complete vortex shedding (Karman vortex). This length of time is adequate for time-averaging in LES of flow around cylinders (Breuer and Hänel, 1993).

Fig. 2 shows the time-averaged streamlines velocities at the upstream and downstream sides of the semi-conical piers at the vertical plane of flow. At the upstream of the piers,

the streamlines are similar, and a small corner vortex (CV) is observed close to the upside of the pier. There are no secondary horseshoe vortices in the time-averaged flow due to the low Reynolds number of the flow around the pier. It should be noted that several secondary horseshoe vortices are present at the upstream of the piers in the instantaneous flow, which are wiped out in the time-averaging process.

As can be observed from Fig. 2, the separation point (saddle point) at the upstream of the pier near the bed gets closer to the upside of the pier with the increase of the side slope angles.

The main flow circulation at the downstream of the cylinder rotates in the anticlockwise direction, and the second one rotates near the bed in a clockwise rotation. For the semi-conical piers at the downstream, the vortices near the bed are smaller than the cylinder. The recirculation length in the wake region is about $1.3D_2 \sim 1.5D_2$ (distance from the center of the piers). These values are consistent with findings in researches of flow around the cylinder (Breuer and Hänel, 1993).

The time-averaged values of the vertical velocities (w) at the up-side of the pier have been compared in Fig. 3. As can be observed from this figure, the magnitude of the down-flow velocity near the bed is gradually decreased by increasing the side slope angles. This reduction is about 25% for the semi-conical pier with $\alpha = 15^\circ$ compared to the cylinder. Further, the attenuation of down-flow velocity may affect the bed shear stress around the piers. Also, with the increase of the side slopes, the up-warding flow can be observed at the upside of the piers. As the down-flow is reduced in front of the pier, the bed shear stress is reduced remarkably.

Fig. 4 shows the normalized time-averaged bed shear stress around the semi-conical piers with different side slopes. The values of the bed shear stresses have been normalized by reference bed shear stress at position $D = 5D_2$ at the upstream side of the piers at the plane of symmetry of the domain. The maximum bed shear stress in the horizontal plane is located at the sides of the piers, as can be observed in this figure. The Large bed shear stress is seen for the cylinder, and the smallest values are observed for the semi-conical pier with $\alpha = 15^\circ$. Then the values of the shear stresses are decreased by increasing the side slopes of the piers. Also, the reduction of bed shear stresses at the sides of the piers is evident. The values of the normalized bed shear stress at the sides of the piers are 17.3, 12.57, 8.83, and 5.8 for the piers with $\alpha = 0^\circ, 5^\circ, 10^\circ$ and 15° , respectively. The reduction of the down-flow velocity and bed shear stress may regard as an important parameter to reduce the sediment transport discharge, and local scour at bridge piers.

The Time-averaged bed shear stress at the symmetry line of the domain at the upstream and downstream of the piers have been compared in Fig. 5. The maximum bed shear stress at this plane occurs in the vicinity of the up-side of the piers. The reduction of the normalized bed shear stress increased with the increase of the side slope of the piers. Reducing the bed shear stress for the pier with $\alpha = 15^\circ$ is about 46% compared to the cylinder. This reduction for the downstream of the pier is about 20%.

Fig. 6 shows the mean (time-averaged) pressure coefficient ($C_p = (p - p_0)/0.5\rho u_0^2$) calculated at the upstream of the piers at the symmetry line of the computational domain where p_0 is the static reference pressure at the inlet of the channel.

Fig. 6.a depicts the C_p along the symmetry line of the flow near the bed. A line sharpness of C_p is observed for all of the piers at $x/D_2 \approx 1.5$ for the cylinder. However, this sharpness gets closer to the pier, with the increase of the side slopes of the semi-conical pier. At this location, the main primary horseshoe vortices are observed. Also, the curve becomes more horizontal with getting distance from the pier at $x/D_2 \approx -4.5$.

Fig. 6.b shows the pressure coefficient across the depth at just close to the upside of the piers. The overall trend of C_p across the depth in Fig. 6.b is similar to the experiment or numerical modeling of flow around pier Dargahi (1989); Roulund et al. (2005) (not shown in this figure). The value of C_p in the present study is slightly higher than the results obtained from the experiment of Dargahi (1989). This discrepancy is due to differences between the pier model properties used in the experiment and the present study, particularly the values of h/D and R_D . The minimum value of C_p for the cylinder is 0.85. C_p is decreased with the increase of α as shown in Fig. 6.b.

4.2 Instantaneous values

4.2.1 Near wake

Cellular behavior of the wake vortices was reported by the researchers for thin and tall tapered cylinders (D Narasimhamurthy et al., 2008; Narasimhamurthy et al., 2009). However, this cellular or multi-cell behavior cannot be observed in the present study due to the bed interaction and the small height of the piers. Oblique vortex shedding is reported by D Narasimhamurthy et al. (2008); Narasimhamurthy et al. (2009) around tapered piers. Williamson (1989) reported some orientation for tall cylinders in wakes. For the tall cylinders, the axes of the vortex tubes are nearly parallel to the cylinder's axis. However, the presence of the free-surface or bed interaction may cause some oblique vortex shedding (Williamson, 1996).

Streamlines of instantaneous flow have been shown in Fig. 7 for the downstream of the piers. The overall flow structure for the cylinder is almost vertical but, for semi-conical piers with the increase of the side slopes, this shedding angle is increased. The angle of inclination concerning the vertical axis for the semi-conical pier with $\alpha = 5^\circ, 10^\circ$ and 15° are about $25^\circ, 37^\circ$ and 45° , respectively. The inclined core axis of the wakes is evident in the flow structure.

The full three-dimensionality of the flow, irregular and intermittent vortex shedding at the downstream of the piers cause highly fluctuating lift ($C_L = F_L/0.5\rho u_0^2 A$) and drag ($C_D = F_D/0.5\rho u_0^2 A$) forces on the cylinder surface (see Fig. 8). Where these coefficients are computed using the pressure and shear stresses acting on the pier surface. The drag coefficient for all the piers is close to 1. This value agrees with other researches about flow around cylinders (Hansen and Forsythe, 2003; Kirkil and Constantinescu, 2015). The lift and drag coefficients show varying amplitude and intensity, hence require substantially long averaging times. Fast Fourier transformation (FFT) was applied to the integrated lift forces.

The power spectrum density of this analysis based on the covariance spectral model is shown in Fig. 9. In this figure, the frequency of vortex shedding is decreased with the increase of the side slopes of the pier. The frequency of the vortex shedding f for semi-conical piers is 1.01, 1.0, 0.92, and 0.83 for the piers with $\alpha = 0^\circ, 5^\circ, 10^\circ$ and 15° , respectively. The most reduction of f is about 18% for the semi-conical pier with $\alpha = 15^\circ$ compared to the cylinder. The rate of the scouring process can be affected by the reduction of the f as mentioned by researchers (Ettema et al., 1998; Fredsoe and Sumer, 2002). Strouhal number for these piers ($St = fD/u_0$) are 0.21, 0.2, 0.19 and 0.17 for the cylinder to semi-conical pier with $\alpha = 15^\circ$, respectively. The value of St for the cylinder is comparable with its found in experiments (Achenbach and Heinecke, 1981; Lienhard et al., 1966).

Fig. 10 depicts the power spectrum density (PSD) of the lift coefficient as a function of frequency. This figure is produced using a snapshot of the flow field, gathered during about eighteen vortex-shedding cycles. The spectrum exhibits a slope close to predicted by

Kolmogorov's theory. This agreement may show that the present LES model has predicted most of the energy in the turbulent scales of the flow.

4.2.2 Horseshoe vortices

The Horseshoe vortex (HV) is generated by the act of the closing boundary layer and down-flow at the upstream side of the pier. The presence of the HV can affect the bed shear stress around the pier. As mentioned by researchers, the HV has an important role in the scour process (Baker, 1980; Dargahi, 1989; Roulund et al., 2005). The structure of the HV is divided into two laminar and turbulent regimes. Different regimes show different behaviors of the HV. These regimes depend on the Reynolds number of the pier, R_D . HV from $R_D = 1000$ to $R_D = 14000$ are classified as laminar HV (Kirkil et al., 2009). Some of the researchers (Greco, 1990; Kirkil and Constantinescu, 2012; Seal et al., 1997) mentioned five sub-regime for the HV system as Steady, Oscillatory, Amalgamating, Break-way, and Transitional sub-regimes. R_D for the present study is about 8000, which lays in the transitional sub-regime.

HV system may be observed from the symmetry plane to the perpendicular plane to the flow. The process of changes for the HVs for the primary HV near the pier is intermittent. For the primary horseshoe vortex (PHV), the alternation is ended with a combination of the PHV and the secondary horseshoe vortex (SHV). The overall shape of the HV is variable in time and cannot be considered as a sustainable form. Comparing horseshoe vortices for the cylinder or the semi-conical piers does not show a significant difference in the number of vortices. However, the size of HVs is different. In the present study, at three points located upstream of the piers (in the x-z vertical plane), the instantaneous velocities have been picked up.

Fig. 11 shows the location of these points. They are located in the area where the horseshoe vortices have the highest spatial variations. The points are located at a distance of about $0.1D_2$ from the bed. In this figure, the primary vortices have shown with PV1 and PV2 and the vortex between the primary vortices are named as the bed vortices BV1 and BV2. These vortices interfere with each other at certain times and become large and small over time due to these instabilities.

The power spectral density analysis over the time variation of the flow velocities for $\alpha = 0^\circ$, and 10° in points 1, 2, and 3 are presented in Fig. 12. As can be observed from Fig. 12-a, for the cylinder, the most energetic peak occurs for point 3. After that, the most robust peaks correspond to points 2 and 1, respectively. The dominant frequency for point 3 is equal to 0.51. The multiple peaks can be observed for point 1. It may show that at this point, temporal changes of the velocity are high. Due to the spatial variations of PV2 and BV1 and the placing of these vortices near point 1, several dominant frequencies are observed in the figure. The frequencies of the HVs for point 3 vary from 0.25 to 2 that are slightly larger than the results obtained in the experiment of Dargahi (1989).

In Fig. 12-b for the cone with $\alpha = 10^\circ$, the most dominant frequency of the HV for all of the points is equal to 0.6. According to this figure, the most energetic oscillation corresponds to point 2. This point is located in the area in which the most robust horseshoe vortex (PV1) is located. Also, for points 2 and 3, some energetic frequencies are observed due to interactions of the HVs. Based on Fig. 12-a and b, the strongest HV for the cylinder has more distance from the pier than the cone. For the cylinder pier, two or more dominant peaks are observed, and for the cone-shaped pier, one energetic peak frequency is observed for all of the points. The dominant frequency of the cone has more energy than that of the cylinder. It may be due to the pier shape and easier vortex formation in front of the cone than the cylinder.

4.3 Conclusion

Results of large eddy simulation of flow around semi-conical piers were presented in this paper. Transient flow passes through the semi-conical piers according to base diameter Reynolds was investigated, and different flow patterns were revealed around them. The most critical modeling result focused on upstream and downstream flow characteristics. It should be noted that the downward flow in the vicinity of the cylinder at the upstream was clear. However, this down-flow velocity was reduced for a tapered pier. The downward flow velocity at the upstream side of the semi-conical piers was decreased by increasing the side slopes. Some of this decrease was due to the increase of side slope, and the remained was due to the decrease in pressure gradient at the pier upstream. Decreasing downward flow velocity reduces bed shear stress. The numerical results showed a remarkable reduction in bed shear stress around the semi-conical pier, especially at the upstream and downstream of the piers. These reductions compared to the corresponding magnitudes of the cylinder were about 46% and 20% at the upstream and downstream, respectively.

Instantaneous flow around the semi-conical piers indicated the oblique vortex shedding behind the piers. The inclination of the vortices was increased with the increase of the side slope of the piers. The integrated lift forces on the semi-conical piers due to vortex shedding showed a dominant frequency. Then, with the increase of the side slopes of the piers, the frequency of vortex shedding was decreased. The time variations of the horseshoe vortices vary at the upstream of the semi-conical piers with different side slopes. The primary vortex had the most significant and more energetic frequencies. Overall results of this study indicated that the flow around the semi-conical pier was different from the cylinder. Some flow behaviors around the semi-conical piers can effectively reduce scour, as mentioned by other researchers in their experiments. The next step of this study will be to study the variation of the Reynolds stresses, turbulent kinetic energy (TKE), and turbulence production behind the pier and the HV system for the semi-conical piers.

Paragraph headings Use paragraph headings as needed.

List of tables

Table 1 Properties of the semi-conical piers.

List of figures

Figure 1 Schematic view of the semi-conical pier.

Figure 2 Time-averaged streamlines using u and w velocities at the up and downstream of the semi-conical piers at the plane of symmetry (flow is from left to right).

Figure 3 Normalized time-averaged vertical velocity (w) at the upstream side of the semi-conical piers.

Figure 4 Time-averaged contours of the normalized bed shear stress around the piers (flow is from left to right).

Figure 5 Time-averaged shear stress at the up and downstream of the semi-conical piers in the plane of symmetry.

Figure 6 Pressure coefficient at the upstream of the pier. (a) Time-averaged pressure at the

upstream of the pier near the bed, (b) Time-averaged pressure at the upside of the pier.

Figure 7 3D instantaneous stream-lines of the flow around the semi-conical pier with different side slopes.

Figure 8 Lift and Drag coefficient of the flow around semi-conical piers. The upper curves correspond to the drag coefficient and the lower correspond to the lift coefficient.

Figure 9 Covariance power spectral density estimate of the lift coefficient of the semi-conical piers with different side slopes.

Figure 10 Power spectrum density of lift coefficient as a function of the frequency in log-log scale. This PSD is given for the semi-conical pier with $\alpha = 10^\circ$.

Figure 11 HV temporal variations upstream of a semi-conical pier.

Figure 12 Power spectral density of velocity change at the upstream of the pier at location of the HVs (a) Cylinder (b) semi-conical pier $\alpha = 10^\circ$.

5 Notation

C_D	= drag force coefficient (-)
C_L	= lift force coefficient (-)
C_p	= pressure coefficient (-)
C_s	= Smagorinsky constant parameter (-)
D	= Mean diameter of the pier (m)
D_1	= diameter of the semi-conical pier at free-surface level(m)
D_2	= diameter of the semi-conical pier at bed level (m)
f	= frequency of vortex shedding (s^{-1})
F_D	= drag force (N)
F_L	= lift force (N)
g	= gravity acceleration (ms^{-2})
h	= flow depth (m)
l_s	= sub-grid length scale (m)
\bar{p}	= filtered pressure (Nm^{-2})
p_0	= static reference pressure (Nm^{-2})
R	= Reynolds number (-)
R_D	= Reynolds number based on the mean diameter of the pier(-)
R_{D_2}	= Reynolds number based on the biggest diameter of the pier(-)
\bar{S}_{ij}	= strain rate tensor for the resolved scale (s^{-1})
St	= Strouhal number (-)
t	= physical time (s)
\bar{u}_i	= filtered velocity (ms^{-1})
u_0	= inlet velocity (ms^{-1})
u_*	= bed shear velocity (ms^{-1})
y	= distance to the nearest wall (m)
z	= distance of the center of the first of wall computational cell (m)
z^+	= non-dimensional distance from the wall based on the shear velocity (-)
α	= Side slope angle of semi conical pier(-)
β	= compressibility parameter (ms^{-1})
Δ	= volume of the computational cell (m^3)
δ_{ij}	= Kronecker delta (-)
κ	= Vonkarman constant (-)
ν	= kinematic eddy-viscosity of fluid (m^2s^{-1})
ν_t	= sub-grid eddy-viscosity (m^2s^{-1})
ρ	= density of fluid (Kgm^{-3})
τ	= virtual time (s)
τ_{ij}	= sub-grid shear stress (Nm^{-2})

6 Declaration

6.1 Author contributions

All authors contributed to the study conception and design. Material preparation, data collection and analysis were performed by Yasin Aghaee-Shalmani and Habib Hakimzadeh. The first draft of the manuscript was written by Yasin Aghaee-Shalmani and all authors

commented on previous versions of the manuscript. All authors read and approved the final manuscript.

Conceptualization: Yasin Aghaee-Shalmani; Methodology: Yasin Aghaee-Shalmani; Formal analysis and investigation: Yasin Aghaee-Shalmani; Writing - original draft preparation: Yasin Aghaee-Shalmani; Writing - review and editing: Yasin Aghaee-Shalmani and Habib Hakimzadeh; Resources: Yasin Aghaee-Shalmani; Software: Yasin Aghaee-Shalmani; Supervision: Habib Hakimzadeh.

6.2 Funding and Conflicts of interests

The authors did not receive support from any organization for the submitted work. No funding was received to assist with the preparation of this manuscript. No funding was received for conducting this study. No funds, grants, or other support was received.

The authors have no relevant financial or non-financial interests to disclose. The authors have no conflicts of interest to declare that are relevant to the content of this article. All authors certify that they have no affiliations with or involvement in any organization or entity with any financial interest or non-financial interest in the subject matter or materials discussed in this manuscript. The authors have no financial or proprietary interests in any material discussed in this article.

References

- Achenbach E, Heinecke E (1981) On vortex shedding from smooth and rough cylinders in the range of reynolds numbers 6×10^3 to 5×10^6 . *Journal of fluid mechanics* 109:239–251
- Afzal MS, Bihs H, Kumar L (2020) Computational fluid dynamics modeling of abutment scour under steady current using the level set method. *International Journal of Sediment Research* 35(4):355–364
- Aghaee Y, Hakimzadeh H (2010) Three dimensional numerical modeling of flow around bridge piers using les and rans. *River Flow 2010* pp 211–218
- Aghaee-Shalmani Y, Hakimzadeh H (2015) Experimental investigation of scour around semi-conical piers under steady current action. *European Journal of Environmental and Civil Engineering* 19(6):717–732
- Aghaee-Shalmani Y, Hakimzadeh H (2016) Numerical modeling of 2-d and 3-d flows using artificial compressibility method and collocated mesh. *Journal of Applied Fluid Mechanics* 9(5):2333–2345
- Baker C (1980) The turbulent horseshoe vortex. *Journal of Wind Engineering and Industrial Aerodynamics* 6(1-2):9–23
- Bozkus Z, Yildiz O (2004) Effects of inclination of bridge piers on scouring depth. *Journal of Hydraulic Engineering* 130(8):827–832
- Breuer M, Hänel D (1993) A dual time-stepping method for 3-d, viscous, incompressible vortex flows. *Computers & fluids* 22(4-5):467–484
- Cheng Y, Lien F, Yee E, Sinclair R (2003) A comparison of large eddy simulations with a standard $k-\epsilon$ reynolds-averaged navier–stokes model for the prediction of a fully developed turbulent flow over a matrix of cubes. *Journal of Wind Engineering and Industrial Aerodynamics* 91(11):1301–1328
- Cubero A, Fueyo N (2007) A compact momentum interpolation procedure for unsteady flows and relaxation. *Numerical Heat Transfer, Part B: Fundamentals* 52(6):507–529

- D Narasimhamurthy V, Andersson HI, Pettersen B (2008) Cellular vortex shedding in the wake of a tapered plate. *Journal of fluid mechanics* 617:355
- Dargahi B (1989) The turbulent flow field around a circular cylinder. *Experiments in Fluids* 8(1):1–12
- Dargahi B (1990) Controlling mechanism of local scouring. *Journal of Hydraulic Engineering* 116(10):1197–1214
- Dey S, Raikar RV (2007) Characteristics of horseshoe vortex in developing scour holes at piers. *Journal of Hydraulic Engineering* 133(4):399–413
- Ettema R, Melville BW, Barkdoll B (1998) Scale effect in pier-scour experiments. *Journal of Hydraulic Engineering* 124(6):639–642
- Fredsøe J, Sumer BM (1997) Scour at the round head of a rubble-mound breakwater. *Coastal engineering* 29(3-4):231–262
- Fredsoe J, Sumer BM (2002) *The mechanics of scour in the marine environment*, vol 17. World Scientific Publishing Company
- Fu WS, Li CG, Lin WF, Chen YH (2009) Roe scheme with preconditioning method for large eddy simulation of compressible turbulent channel flow. *International journal for numerical methods in fluids* 61(8):888–910
- Gazi AH, Afzal MS (2020) A review on hydrodynamics of horseshoe vortex at a vertical cylinder mounted on a flat bed and its implication to scour at a cylinder. *Acta Geophysica* 68:861–875
- Greco JJ (1990) *The flow structure in the vicinity of a cylinder-flat plate junction: flow regimes, periodicity, and vortex interactions*. PhD thesis, Lehigh University
- Guan D, Chiew YM, Wei M, Hsieh SC (2019) Characterization of horseshoe vortex in a developing scour hole at a cylindrical bridge pier. *International journal of sediment research* 34(2):118–124
- Gushchin V, Kostomarov A, Matyushin P, Pavlyukova E (2002) Direct numerical simulation of the transitional separated fluid flows around a sphere and a circular cylinder. *Journal of Wind Engineering and Industrial Aerodynamics* 90(4-5):341–358
- Hansen R, Forsythe J (2003) Large and detached eddy simulations of a circular cylinder using unstructured grids. In: *41st Aerospace Sciences Meeting and Exhibit*, p 775
- Hsiao F, Pan J, Chiang C (1993) The study of vortex shedding frequencies behind tapered circular cylinders. *ASME-PUBLICATIONS-PVP* 245:103–103
- Hsiao FB, Chiang CH (1998) Experimental study of cellular shedding vortices behind a tapered circular cylinder. *Experimental thermal and fluid science* 17(3):179–188
- Khosla P, Rubin S (1974) A diagonally dominant second-order accurate implicit scheme. *Computers & Fluids* 2(2):207–209
- Kim WW, Menon S (1999) An unsteady incompressible navier–stokes solver for large eddy simulation of turbulent flows. *International Journal for Numerical Methods in Fluids* 31(6):983–1017
- Kirkil G, Constantinescu G (2012) A numerical study of the laminar necklace vortex system and its effect on the wake for a circular cylinder. *Physics of Fluids* 24(7):073602
- Kirkil G, Constantinescu G (2015) Effects of cylinder reynolds number on the turbulent horseshoe vortex system and near wake of a surface-mounted circular cylinder. *Physics of Fluids* 27(7):075102
- Kirkil G, Constantinescu S, Ettema R (2008) Coherent structures in the flow field around a circular cylinder with scour hole. *Journal of Hydraulic Engineering* 134(5):572–587
- Kirkil G, Constantinescu G, Ettema R (2009) Detached eddy simulation investigation of turbulence at a circular pier with scour hole. *Journal of Hydraulic Engineering* 135(11):888–901

- Kitagawa T, Ohta H (2008) Numerical investigation on flow around circular cylinders in tandem arrangement at a subcritical reynolds number. *Journal of Fluids and Structures* 24(5):680–699
- Labbé D, Wilson P (2007) A numerical investigation of the effects of the spanwise length on the 3-d wake of a circular cylinder. *Journal of Fluids and Structures* 23(8):1168–1188
- Lam K, Lin Y (2008) Large eddy simulation of flow around wavy cylinders at a subcritical reynolds number. *International Journal of Heat and Fluid Flow* 29(4):1071–1088
- Lienhard JH, et al. (1966) Synopsis of lift, drag, and vortex frequency data for rigid circular cylinders, vol 300. Technical Extension Service, Washington State University Pullman, WA
- Nagata N, Hosoda T, Nakato T, Muramoto Y (2005) Three-dimensional numerical model for flow and bed deformation around river hydraulic structures. *Journal of Hydraulic Engineering* 131(12):1074–1087
- Narasimhamurthy VD, Andersson HI, Pettersen B (2009) Cellular vortex shedding behind a tapered circular cylinder. *Physics of Fluids* 21(4):044106
- Olsen NR, Melaaen MC (1993) Three-dimensional calculation of scour around cylinders. *Journal of Hydraulic Engineering* 119(9):1048–1054
- Ouro P, Wilson CA, Evans P, Angeloudis A (2017) Large-eddy simulation of shallow turbulent wakes behind a conical island. *Physics of Fluids* 29(12):126601
- Paik J, Escarriaza C, Sotiropoulos F (2007) On the bimodal dynamics of the turbulent horseshoe vortex system in a wing-body junction. *Physics of Fluids* 19(4):045107
- Pourahmadi M, Hakimzadeh H (2011) Experimental investigation of local scour around conical pier. In: *International Conference on Offshore Mechanics and Arctic Engineering*, vol 44380, pp 351–355
- Rodi W (1997) Comparison of les and rans calculations of the flow around bluff bodies. *Journal of wind engineering and industrial aerodynamics* 69:55–75
- Rodi W (2006) Dns and les of some engineering flows. *Fluid Dynamics Research* 38(2-3):145
- Roulund A, Sumer BM, Fredsøe J, Michelsen J (2005) Numerical and experimental investigation of flow and scour around a circular pile. *Journal of Fluid Mechanics* 534:351
- Salaheldin TM, Imran J, Chaudhry MH (2004) Numerical modeling of three-dimensional flow field around circular piers. *Journal of Hydraulic Engineering* 130(2):91–100
- Seal C, Smith C, Rockwell D (1997) Dynamics of the vorticity distribution in endwall junctions. *AIAA journal* 35(6):1041–1047
- Sheu TW, Lin RK (2004) Newton linearization of the incompressible navier–stokes equations. *International Journal for Numerical Methods in Fluids* 44(3):297–312
- Sumer B, Fredsøe J, Christiansen N, Hansen S (1995) Bed shear stress and scour around coastal structures. In: *Coastal Engineering 1994*, pp 1595–1609
- Unger J, Hager WH (2007) Down-flow and horseshoe vortex characteristics of sediment embedded bridge piers. *Experiments in Fluids* 42(1):1–19
- Vaghefi M, Ghodsian M, Salimi S (2016) The effect of circular bridge piers with different inclination angles toward downstream on scour. *Sadhana* 41(1):75–86
- Williamson C (1989) Oblique and parallel modes of vortex shedding in the wake of a circular cylinder at low reynolds numbers. Tech. rep., CALIFORNIA INST OF TECH PASADENA GRADUATE AERONAUTICAL LABS
- Williamson CH (1996) Vortex dynamics in the cylinder wake. *Annual review of fluid mechanics* 28(1):477–539
- Zhang W, Zapata MU, Bai X, Pham-Van-Bang D, Nguyen KD (2020) Three-dimensional simulation of horseshoe vortex and local scour around a vertical cylinder using an unstruc-

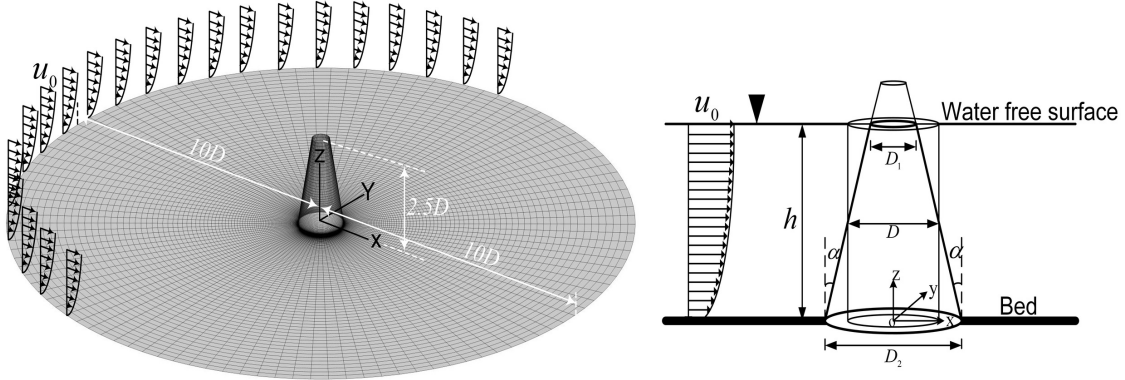
tured finite-volume technique. *International Journal of Sediment Research* 35(3):295–306

7 Tables

8 Figures

Table 1 Properties of the semi-conical piers.

Side slope α°	$D(m)$	$D_1(m)$	$D_2(m)$	$h(m)$	FlowVelocity(ms^{-1})
0	0.04	0.04	0.04	0.1	0.19
5.0	0.04	0.03125	0.04875	0.1	0.19
10.0	0.04	0.02237	0.05763	0.1	0.19
15.0	0.04	0.01312	0.06679	0.1	0.19

**Fig. 1** Schematic view of the semi-conical pier.

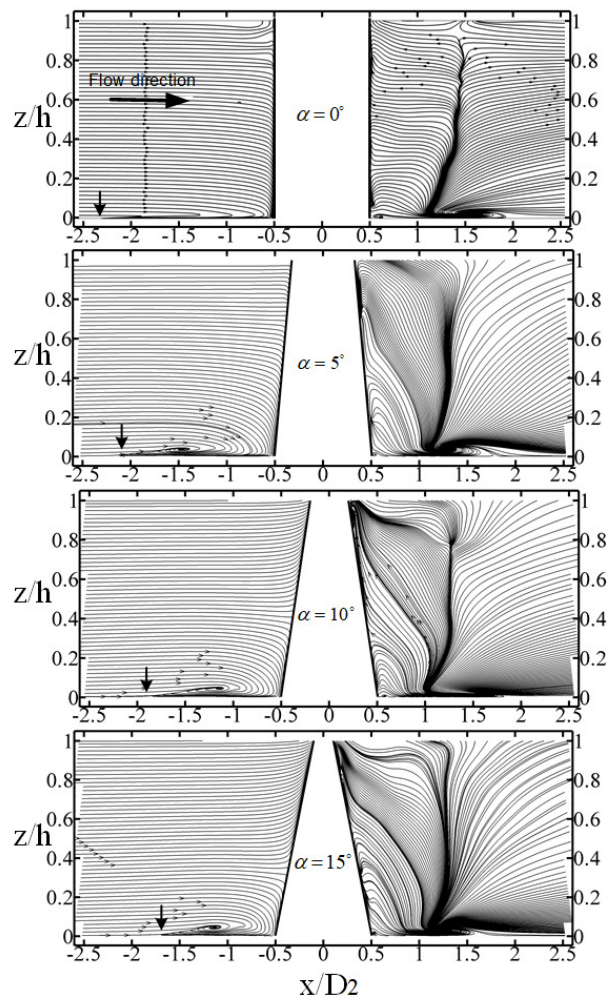


Fig. 2 Time-averaged streamlines using u and w velocities at the up and downstream of the semi-conical piers at the plane of symmetry (flow is from left to right).

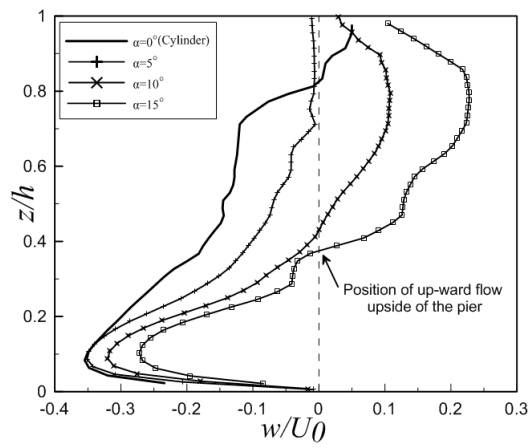


Fig. 3 Normalized time-averaged vertical velocity (w) at the upstream side of semi-conical piers

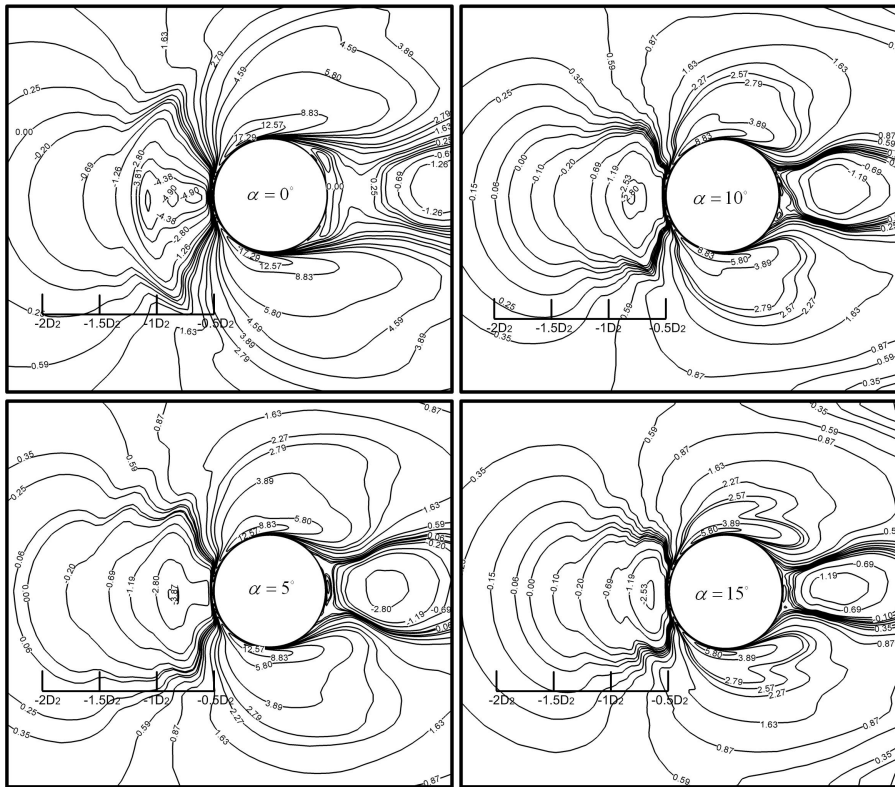


Fig. 4 Time-averaged contours of the normalized bed shear stress around the piers (flow is from left to right).

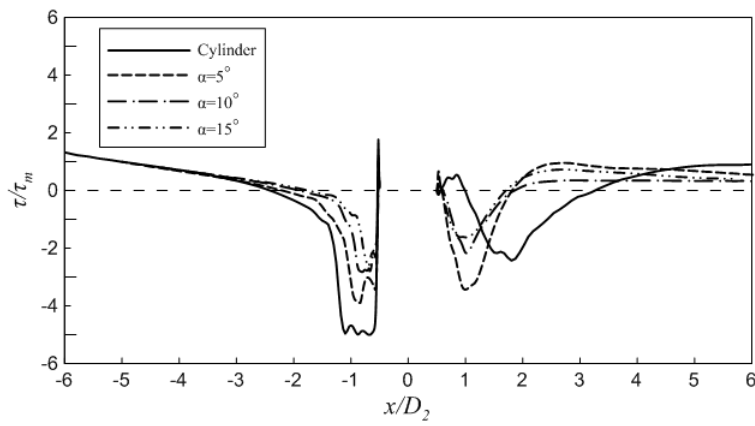


Fig. 5 Time-averaged shear stress at the up and downstream of the semi-conical piers in the plane of symmetry.

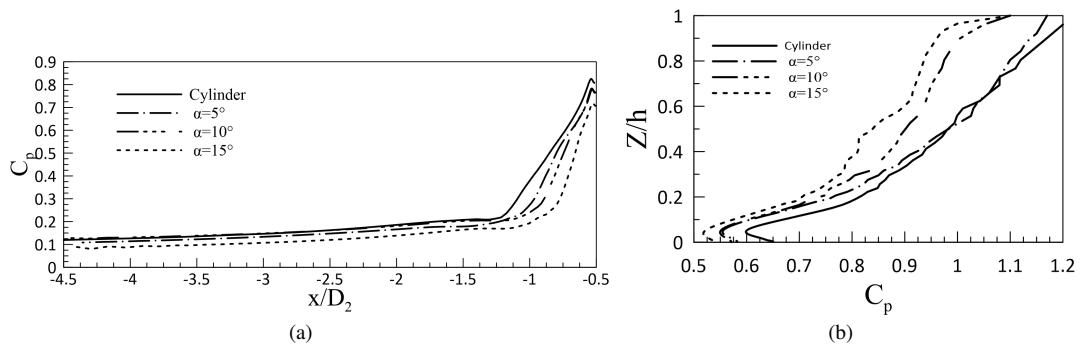


Fig. 6 Pressure coefficient at the upstream of the pier. (a) Time-averaged pressure at the upstream of the pier near the bed, (b) Time-averaged pressure at the upside of the pier.

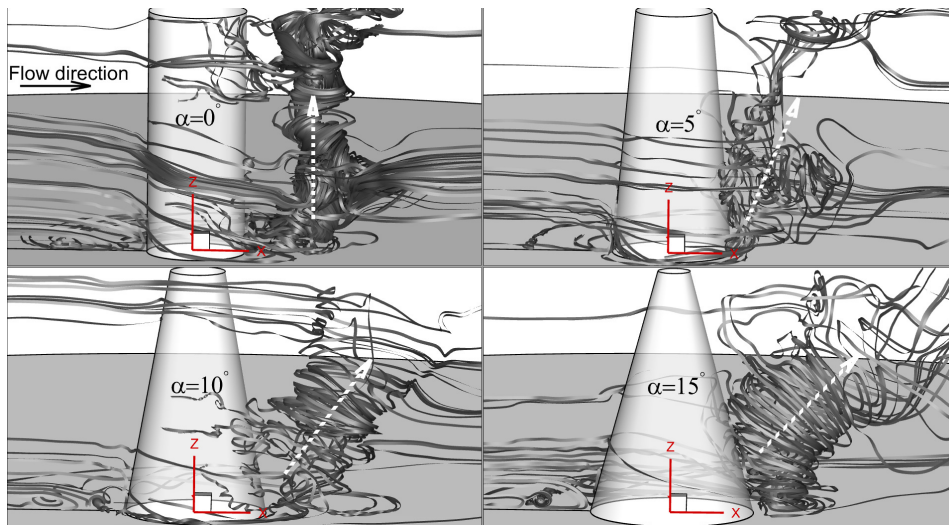


Fig. 7 3D instantaneous stream-lines of the flow around the semi-conical pier with different side slopes.

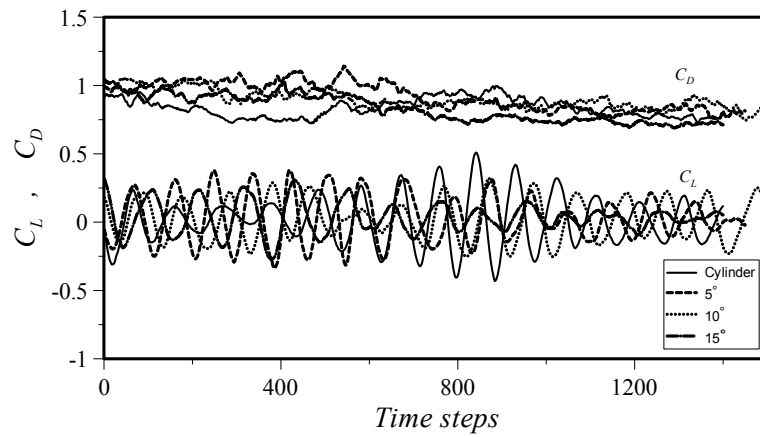


Fig. 8 Lift and Drag coefficient of the flow around semi-conical piers. The upper curves correspond to the drag coefficient and the lower correspond to the lift coefficient.

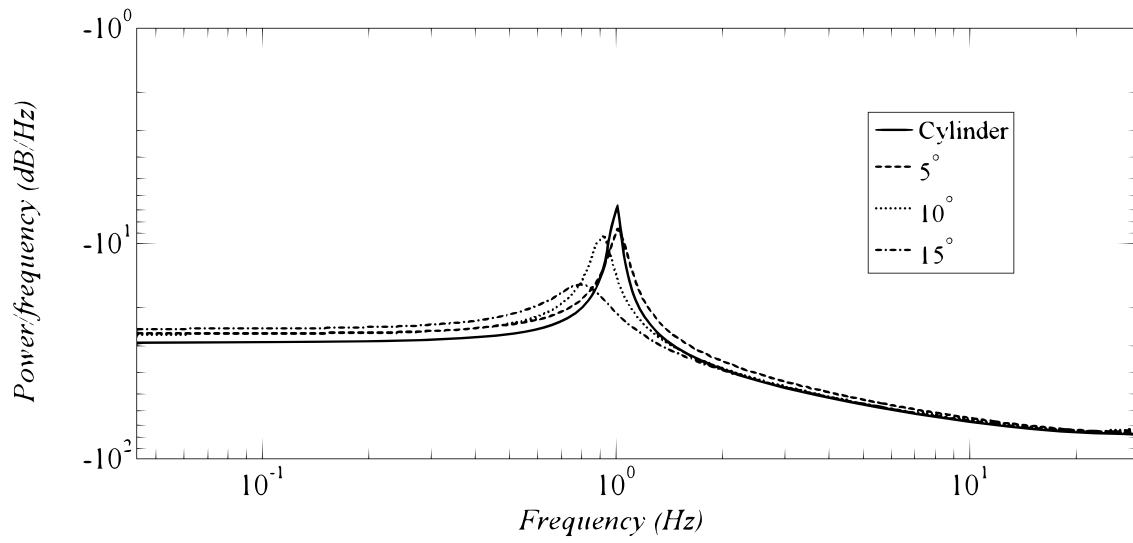


Fig. 9 Covariance power spectral density estimate of the lift coefficient of the semi-conical piers with different side slopes.

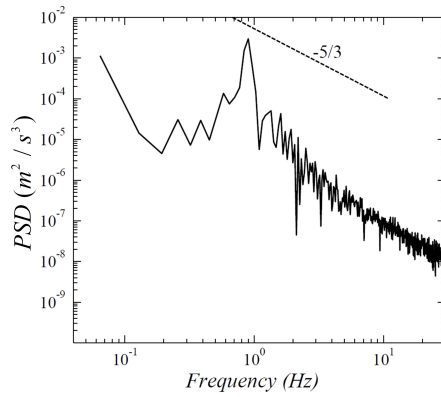


Fig. 10 Power spectrum density of lift coefficient as a function of the frequency in log-log scale. This PSD is given for the semi-conical pier with $\alpha = 10^\circ$.

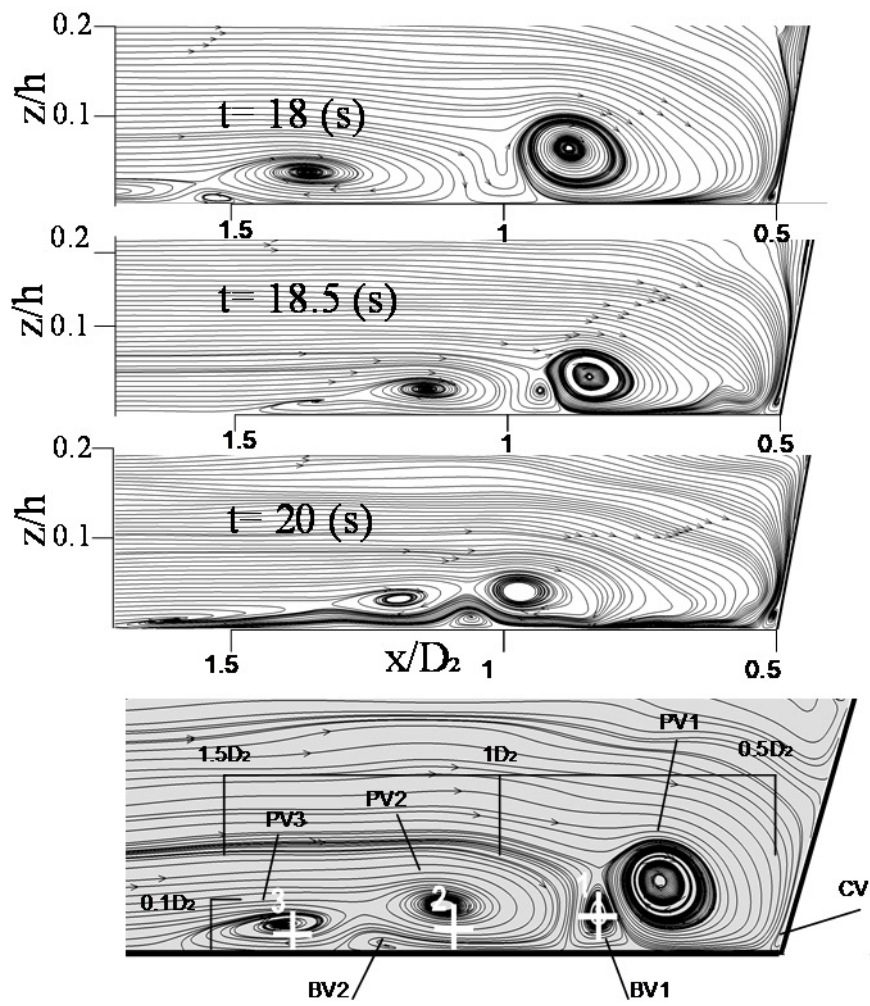


Fig. 11 HV temporal variations upstream of a semi-conical pier

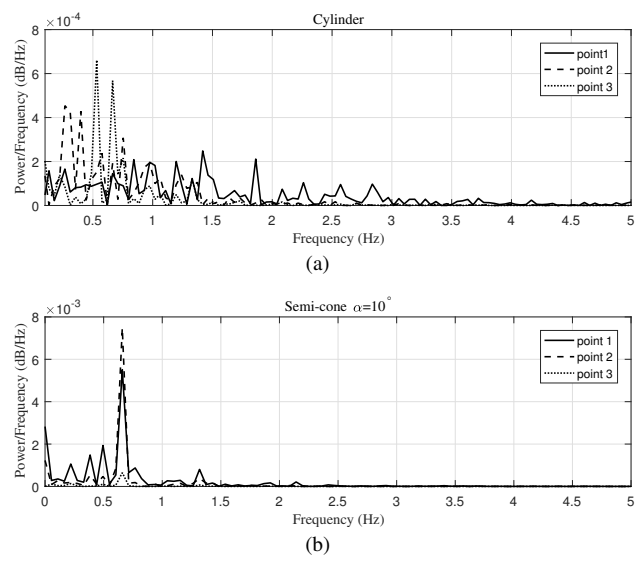


Fig. 12 Power spectral density of velocity change at the upstream of the pier at location of the HVs (a) Cylinder (b) semi-conical pier ($\alpha = 10^\circ$).